Nanoscale chemistry and ion segregation in zirconia-based ceramic at grain boundaries by atom probe tomography

Olivia G. Licata[a], Menglin Zhu[b], Jinwoo Hwang[b], Baishakhi Mazumder[a*]

[a] Department of Materials Design and Innovation, University at Buffalo, The State University of New York, Buffalo, NY 14260, United States

[b] Department of Materials Science and Engineering, The Ohio State University, Columbus, OH 43210, United States

* Correspondence: baishakh@buffalo.edu

Abstract

In this work nanoscale features that are of importance in the stability of yttria-stabilized tetragonal zirconia (Y-TZP) are quantified through atom probe tomography. In-depth analysis of grain boundary chemistry revealed preferential segregation of lighter and smaller ions towards specific grain boundaries. The relationship between elemental segregation and the local atomistic structure is investigated at the sub-nanometer level to gain insights on nanoscale features associated with the tetragonal-monoclinic phase transformation in Y-TZP through grain boundary characterization. Principal component analysis was implemented to reveal any potential biases from varied field evaporation across stabilizer-rich grain boundaries. The observed variations in ion density across different grains suggested a variation in field which was attributed to potential variations in grain crystal orientation. In order to reveal the subtle depletion of oxygen atoms within grain boundaries a new methodology to map oxygen vacancies is proposed, utilizing the relative neighborhood chemistry of individual yttrium atoms.

~~Zirconia (ZrO₂) ceramics outperform alternative material systems and are more resistant to crack~~ ~~growth than other ceramics due to their unique transformation-toughening mechanism [1-3]. The~~ ~~addition of stabilizing aliovalent oxides, such as Yttria (Y₂O₃) stabilized zirconia lowers the~~ ~~tetragonal to monoclinic (t-m) phase transformation temperature and allows zirconia to be~~ ~~implemented as a bulk structural material [4-6].~~ The yttria-stabilized tetragonal zirconia polycrystals (Y-TZP) ~~system is characterized by 1-3 mol.% of yttria and has been~~ are referred ~~to~~ as "ceramic steel" due to its high mechanical strength (>1 GPa) and excellent fracture toughness (4-6 MPa*m$^{1/2}$) [7, 8]. Despite this claim, there are still limitations in the long-term strength and mechanical stability of Y-TZP due to tetragonal to monoclinic (t-m) phase transformation [9]. The t-m phase transformation is associated with a 3-4% volume expansion, which induces compressive strains that work to inhibit further crack propagation [3, 10-12]. Ageing-induced t-m transformation has previously been investigated in relation to processing parameters such as the sintering temperature, grain size, and stabilizer content [13, 14]. However, there is a need for detailed analysis that incorporates the insights from nanoscale chemistry, to link processing parameters with microstructural features associated with the t-m transformation.

Grain boundaries (GBs) are believed to be the nucleation site for the t-m transformation and the path for transformation to propagate during degradation [15, 16]. Reducing the average grain size in Y-TZP is often associated with improved stability; however, smaller grains result in more potential GBs, which is kinetically favorable for phase transformation [17]. Previous studies have incorporated varying dopant systems, such as alumina (Al₂O₃), to engineer GBs to improve ageing resistance without reducing the resistance to crack propagation in Y-TZP [1, 18]. Experimental reports have shown segregation of stabilizer, dopant, and impurity species towards GBs in Y-TZP [19-25]. The substitution of yttria into the zirconia sublattice introduces one oxygen vacancy (V_O)

for every pair of yttrium (Y) ions [21, 26]. The annihilation of V_Os is widely accepted as the major mechanism of the ageing-induced t-m transformation [21, 27-30], however, current methods for quantifying V_Os rely on indirect measurements of ionic conductivity or photoluminescence bands [21, 31]. Space charge theory predicts that the GB core is positively charged with adjacent V_O-depleted space-charge layers approximately 2.5 nm thick [7, 21, 32, 33]. Recently, direct experimental characterization of relative O concentration across GBs indicated a depletion of V_Os near the GB cores [34]. Contradictory findings from theoretical and experimental results demonstrate that there is a need for verification of O distribution relative to GBs [34-37]. Despite the previous effort to understand the t-m transformation, direct experimental evidence of quantitative local chemistry, associated defects, and defect complexes that cause the phase transformation is missing. In the current work, characteristics of grains and GBs are reported at the micro- and nano-scale levels using scanning transmission electron microscopy (STEM) and atom probe tomography (APT), respectively. Further, a new methodology for mapping V_Os is presented to reveal the subtle depletion of oxygen atoms within GBs. The in-depth analysis reported here provides necessary insights on the atomic-level relations between features associated with phase transformation in Y-TZP (GBs and V_Os).

The test structure is a commercially available tetragonal zirconia (IPS e.max ZirCAD LT, Ivoclar Vivadent), with 3 mol.% yttria stabilizer (3Y-TZP). STEM provided the micrometer-level investigation, including high resolution imaging for grain size distribution. APT facilitated the nanometer-level investigation of GBs, including stabilizer segregation and mapping of V_Os. Principal component analysis (PCA) was implemented to reveal any potential biases from varied field evaporation across stabilizer-rich GBs [38, 39]. Additionally, PCA scores are visually represented within the region of interest to demonstrate the variation in features associated with

field evaporation. This revealed the potential influence of grain orientation, grain boundaries, and elemental segregation on relative field evaporation. Further details on the experimental methods are included in the Supplementary documentation.

The grain size defines the microstructure and provides insights relating to the overall stability [17]. STEM images were used to obtain the distribution of grain size and microstructural chemistry. The approximate areas for grains were obtained from multiple regions of the 3Y-TZP sample using the Materials Image Processing and Automated Reconstruction (MIPAR) software. A representative region of grains is shown in Figure 1(a) with its corresponding color-coded grain size map in Figure 1(b). The distribution of grain size taken from 5 different images is reported in Figure 1(c). The average grain area was 0.09 µm^2, corresponding to an average diameter of 0.31 µm. Next, STEM with energy dispersive X-ray (EDX) spectroscopy and high-angle annular dark-field (HAADF) images were acquired along a single GB in Figure 1(d), revealing a decrease in Zr and an increase in O from Grain A towards Grain B in Figure 1(e). This suggests potential variation in chemistry between different grains within 3Y-TZP. Additionally, increased concentrations of Y and Al observed at the GB indicate segregation of stabilizer content and impurities towards the GB.

To investigate the variations in local chemistry between grains and GBs, APT was employed for its sub-nanometer level elemental characterization. For improved statistical significance, data from two APT sample tips are included in the following analysis (from here on referred to as S1 and S2). A scanning electron microscopy (SEM) image of the 3Y-TZP GBs is included in Figure 2(a) to demonstrate the region of a triple junction used for S1 and a GB edge used for S2. The three-dimensional (3D) atom maps acquired through APT are shown in Figure 2(b), where each orange point represents a single Y atom. The dark orange volumes correspond to Y-rich GBs, which were

generated using the CAMECA, Inc. Integrated Visualization Analysis Software. The major GBs are labeled in Figure 2(b) for S1 and S2. The corresponding mass spectrum from APT, shown in Figure 2(c), revealed unintentional impurities, including aluminum (Al), silicon (Si), and hafnium oxide (HfO). The presence of Hf impurities in zirconia is unavoidable, as zirconium itself is always found with 1-3 wt.% Hf [40]. The level of Al observed (0.05 at.%) is at trace levels and is expected in the commercial 3Y-TZP. To investigate the 3D distribution of Al relevant to GBs, one-dimensional concentration profiles (1DCPs) were taken along cylindrical volumes (diameter = 15 nm) perpendicular to each GB. As demonstrated by the 1DCPs in Figure 2(d), S1-GB1 has increased Al within the core of the Y-rich GB; however, S1-GB4 does not demonstrate any segregation of Al. In addition to the chemical variation between GBs, the GB profiles demonstrate varied thickness, indicated by the full width at half maximum (FWHM) values in Figure 2(d).

To distinguish between GB characteristics and any potential artifacts, PCA was performed on a set of variables associated with field evaporation. Y-TZP is an inhomogeneous crystal ceramic with known complex features, such as GBs, which can demonstrate varied composition, thickness, and orientation. These variations can modify the field evaporation during APT acquisition leading to uncertainty in the resulting structure-chemistry analysis [41]. Parameters chosen for the APT acquisition were optimized; however, given the known complex features within the inhomogeneous Y-TZP ceramic, some variation is unavoidable. Implementing PCA allows for dimensionality reduction of the atomic-level dataset and provides an indication of each input feature's contribution to variability, thereby revealing potential correlations, biases, and relevant features [42, 43]. The region of interest selected for PCA was a 50 x 50 x 5 nm^3 volume, capturing the triple junction in S1. The input features are listed and defined in Table 1 along with the results of PCA. The feature associated with the greatest contribution to variability was ΔP, with 63.2%.

The next highest contribution was 18.9% from like-NN, but this is attributed to the segregation of elements at the GBs. The contribution from RSS can be disregarded as it is only a function of position. The remaining features, TOF and V_{DC} had minimal contribution to the variability.

To define the extent of potential bias, the spatial variation of these features was investigated. The region of interest (ROI) used for PCA is shown in Figure 3(a), with all Y and Al atoms displayed. The density of total detected ions was collected from 2 x 2 x 5 nm^3 voxels within the ROI and plotted in Figure 3(b), where the highest density zones are red and the lowest density zones are blue. The scores (values projected into eigenspace) from PC1 and PC2 are plotted in Figures 3(c) and 3(d), respectively. The mapping of the density of ions in Figure 3(b) indicates that the GBs have a higher density of ions, but also suggests that Grain C has a lower density of ions than Grain A and Grain B. The observed variation in density does not align with the bias associated with the laser-heated side of the sample. The reduced density of ions in Grain C could be due to a variation in field evaporation associated with a change in grain orientation, relative to the neighboring grains [41]. This inhomogeneity is somewhat unavoidable, considering the polycrystalline nature of Y-TZP, however, this variation in density did not hinder the elemental quantification within the observed grains or GBs in the dataset. PC1, corresponding to ΔP, demonstrated the highest contribution to variability; however, the distribution relative to the triple junction grains is homogeneous in Figure 3(c). This suggests that the variability in ΔP detected by PCA was not a result of physics but is rather corresponding to noise. The scores from PC2, corresponding to the like-NN distance in Figure 3(d) demonstrated an inverse relationship with the density of ions from Figure 3(b). This is somewhat intuitive, as regions with a lower density of ions will have larger separation distances between events, thereby resulting in larger values for like-NN. These findings

helped elucidate inhomogeneities in the material, to allow for accurate quantification of the grains and GBs.

After verifying that the changes in field evaporation were minimal and did not bias the observed segregation to GBs, the GB characterization was carried out confidently. Characteristics for the six major GBs from S1 and S2 are tabulated in Table 2, including elemental composition and GB thickness. Within GBs the Zr at.% reduces while the Y at.% increases, indicating increased substitution of Y^{3+} for Zr^{4+}. As shown in Table 2, GBs with higher Y concentration (4-5 at.%) demonstrate a tendency towards greater thickness (7-11 nm) compared to the other Y-rich GBs. S1-GB1 and S2-GB2 demonstrated preferential segregation of Al and Si. Interestingly, the GBs with Al and Si segregation have less Y and are thinner than the other Y-rich GBs, suggesting an interrelation between the chemical and physical properties of GBs. Compared to the bulk composition of samples, the concentration of O and Hf within GBs appears similar.

To better understand the 3D distribution of elements relative to the GBs, 2D concentration profiles were taken in three planes around the GBs. In Figure 4, two GBs were selected for comparison, an Al-rich S1-GB1 in Figure 4(a) and an Y-rich S1-GB4 in Figure 4(b). S1-GB1 in Figure 4(a) demonstrates the segregation of Al and Si to the Y-rich GB in the xy-plane, but not the GB perpendicular to it (GB 2). There is also no indication of Al or Si segregation shown in Figure 4(b) for S1-GB4. The observed preferential segregation in S1-GB1 could be a result of lighter and smaller ions like Al and Si diffusing interstitially, compared to the slower process of Y^{3+} substituting Zr^{4+} [44]. Previous investigations on high-temperature plastic deformation in Y-TZP confirmed that Zr and Y are the slowest moving species [45, 46]. Additionally, the diffusion mechanism of Al^{3+} within the GB diffusion is much slower than within the bulk grain [47]. Both diffusion routes will result in strengthened GBs since the segregated ions will form strong bonds

with the V_Os [21, 32]. Strong GBs were previously exemplified through the predominant occurrence of transgranular fracture (as opposed to intergranular fracture) at the surface of alumina-doped (0.05 and 0.25 wt%) 3Y-TZP [21].

The segregation of yttria to GBs and the positive charge of the GB core suggest that the GB has an enhanced concentration of V_Os [32]. Here, the atomic concentration of O is utilized as a direct measure of V_Os, indicated by depletion of O [48]. In Figure 4, the Y-rich GBs have been outlined in magenta to aid the visualization of potential O depletion. Ionic concentration profiles indicated a decrease in ^{16}O and ZrO at the GBs. The depletion of overall (decomposed) O content at the GBs is not significantly visible in Figure 4 and may be too subtle to observe in this manner. Here, a new methodology is proposed for mapping V_Os in which a pseudo-coordination number (p-CN) is defined for each Y atom. The coordination number refers to the number of atoms, molecules, or ions bonded to the central atom. The unit cell of yttria has a cubic structure with one Y atom in the center and 8 corners including 6 O atoms and 2 vacancies. The methodology is schematically shown in Figure 5a, where 8 nearest neighbors of the central Y atom are indicated with arrows. The p-CN defined here will rely on APT data which does not detect 100% of the atoms from the original structure. For this reason, p-CN is a relative measure for regions of likely O-depletion. In Figure 5b, the ROI captures the same triple junction area (XZ plane) as Figure 3, but with a thicker y-dimension (8 nm). Here, each point is a Y atom, and the color is an indication of how many of its nearest neighbors contain O. The right-most image in Figure 5b provides a close-up of the boxed region at the triple junction where several O-depleted Y atoms are observed. Colors corresponding to fewer O neighbors (red, magenta, and green) are likely zones for V_Os. There is a clear trend in O-depletion within the GBs that was previously more difficult to detect via composition profiles. The composition profile, which relies on an average taken perpendicular to

the GB, could be influenced by the of V_Os within the space-charge layer of the GB, which is typically one-half of the thickness of the GB core [32]. Figure 5b also suggests that there is more depletion of O within Al-rich GB1 than the Y-rich GB2. Due to the trivalent nature of Al, there may be a higher concentration of V_Os accommodated at the interface of alumina and zirconia than within the grain [49, 50], which is associated with improved stability of the t phase [50].

In this work, the relationship between elemental segregation and the local atomistic structure was directly shown through 3D compositional analysis at the sub-nanometer level, providing insights on features associated with the t-m transformation and subsequent ageing in Y-TZP. PCA was implemented to reveal potential biases from varied field evaporation across the inhomogeneous ceramic structure. An in-depth analysis of GB chemistry revealed preferential segregation of light element impurities to specific GBs. The subtle depletion of O atoms within GBs was not significantly visible in standard composition profiles. Here a new methodology to map V_Os was implemented, utilizing the relative neighborhood chemistry of individual Y atoms. This work establishes the foundation for understanding atomic scale interaction between GB and chemical species that plays a significant role in material degradation and can be employed to comprehend t-m transformation mechanisms.
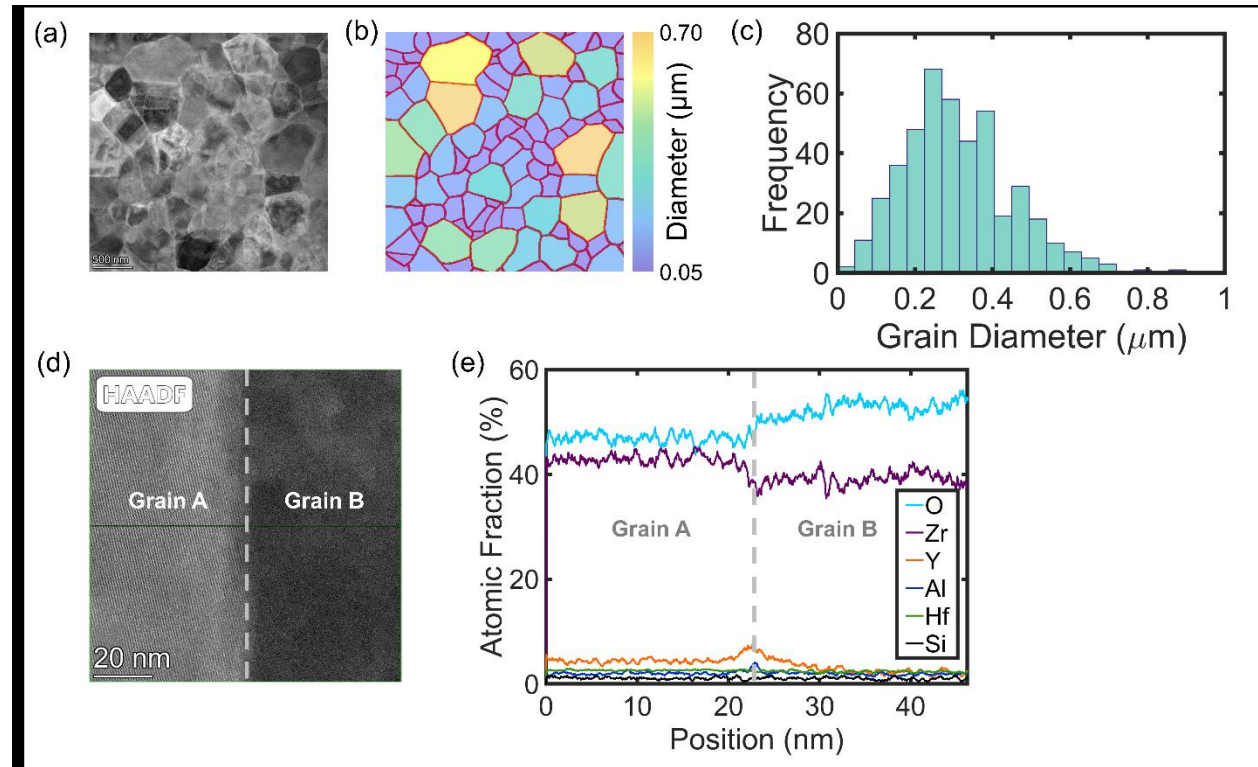
Figures

Figure 1: (a) LAADF image of grains from a representative region and its corresponding (b) grain size map. (c) Distribution of grain diameters from five different images. (d) EDX with atomic-resolution HAADF image of a single GB with corresponding (e) composition profile.
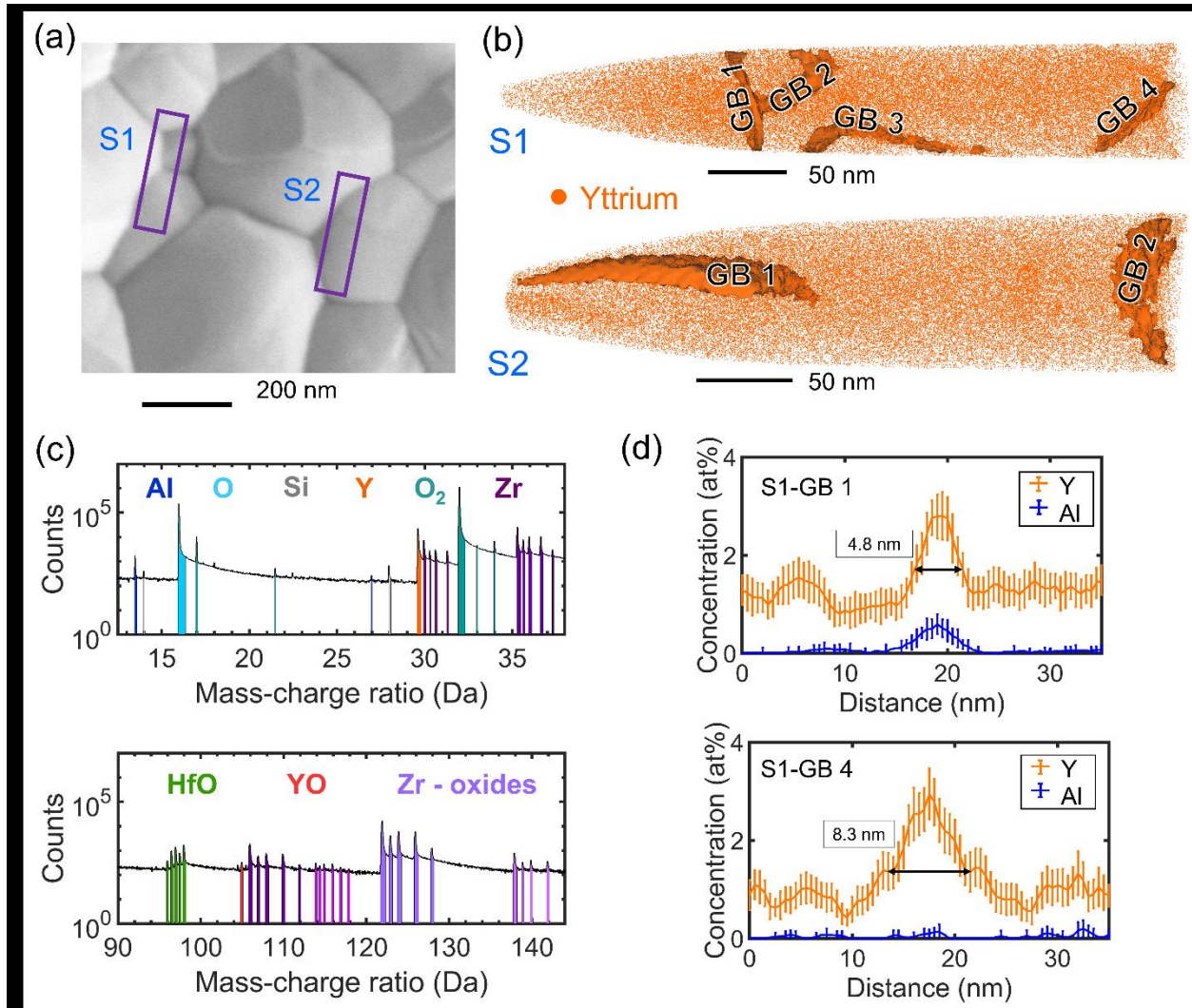
Figure 2: (a) SEM image of GB regions, (b) 3D atom maps of Y in S1 and S2 with iso-surfaces capturing GBs with more than 1.9 at.% Y. (c) Mass spectra for 3Y-TZP. (d) 1-D line profiles taken perpendicular to GB 1 (upper) and GB 4 (lower) from S1 with full-width half-maxima values indicated. Cylinders for the line profiles had cross-sections with 15 nm diameters.
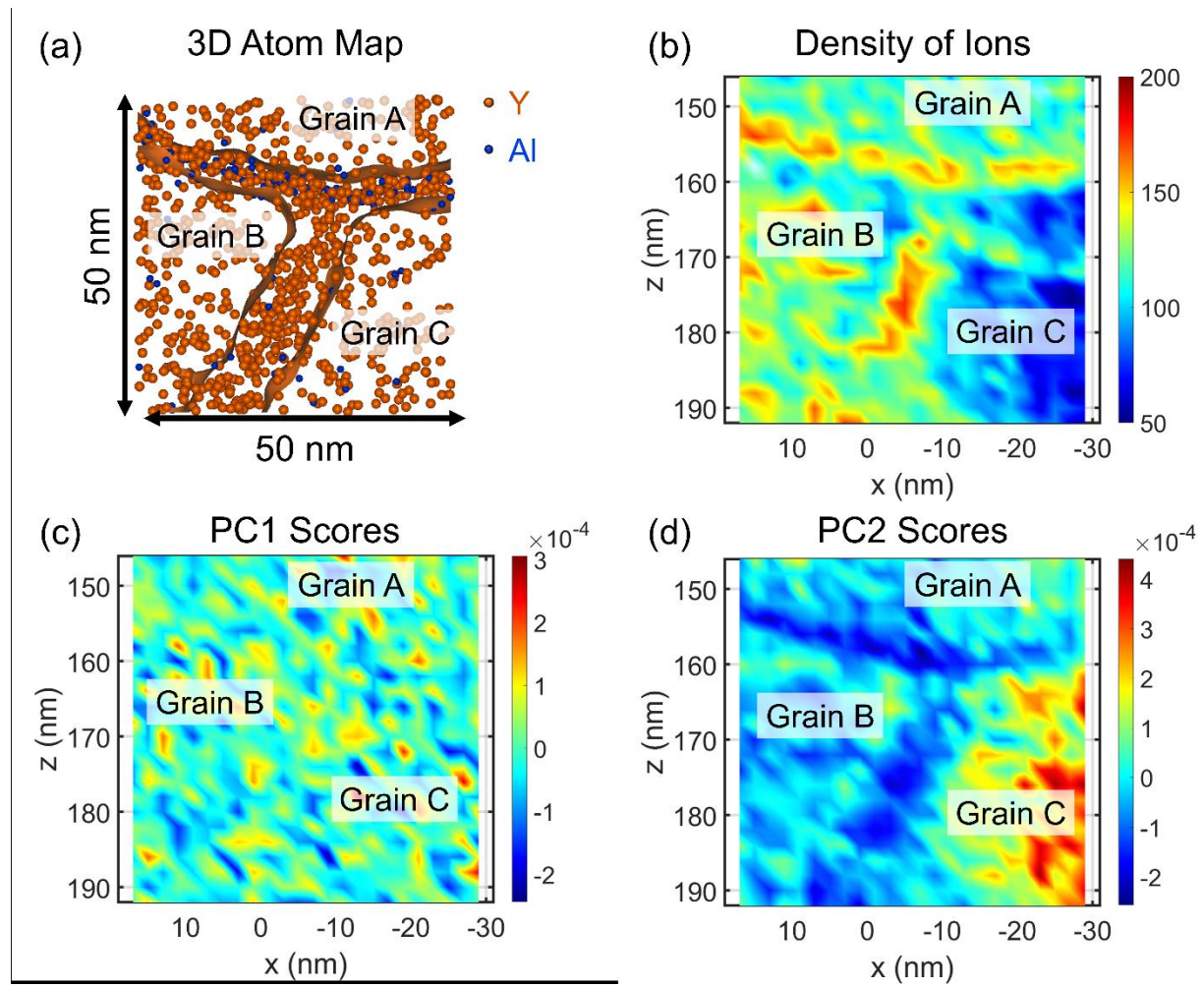
Figure 3: (a) 50 x 50 x 5 nm³ ROI used for PCA, with all Y and Al atoms displayed, where the upper Al-rich GB and the lower Y-rich GB form a triple junction of three neighboring grains: Grain A, B, and C. (b) Density of detected ions within the ROI and PC scores corresponding to (c) ΔP and (d) like-NN features.
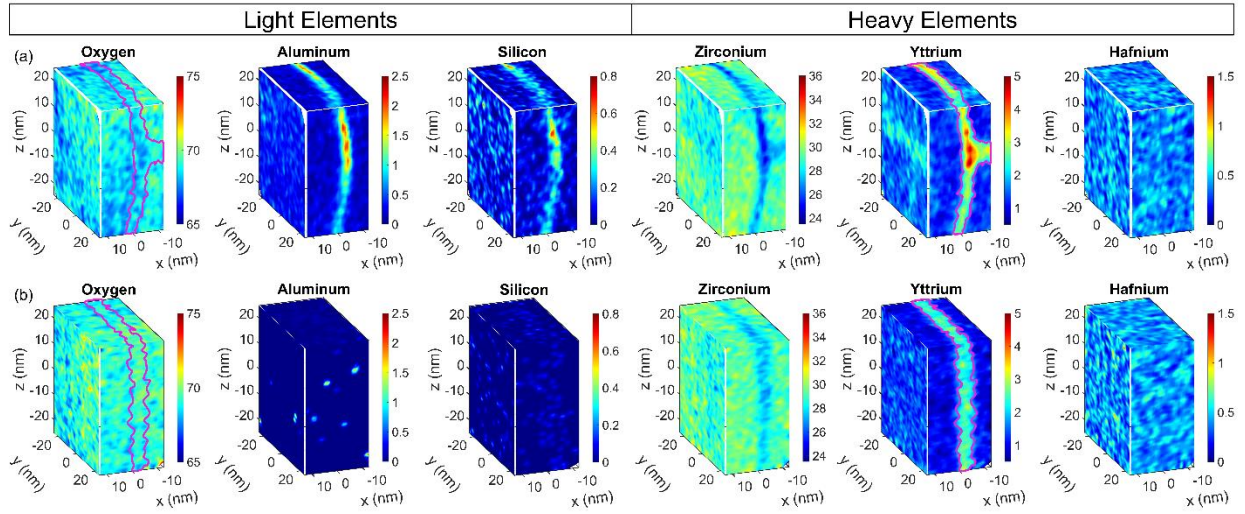
Figure 4: Three planes of 2D concentration profiles for light elements (O, Al, and Si) and heavy elements (Zr, Y, and Hf) within (a) GB 1 and (b) GB 4 from S1. Y-rich GBs in the xy and xz planes are outlined in magenta.
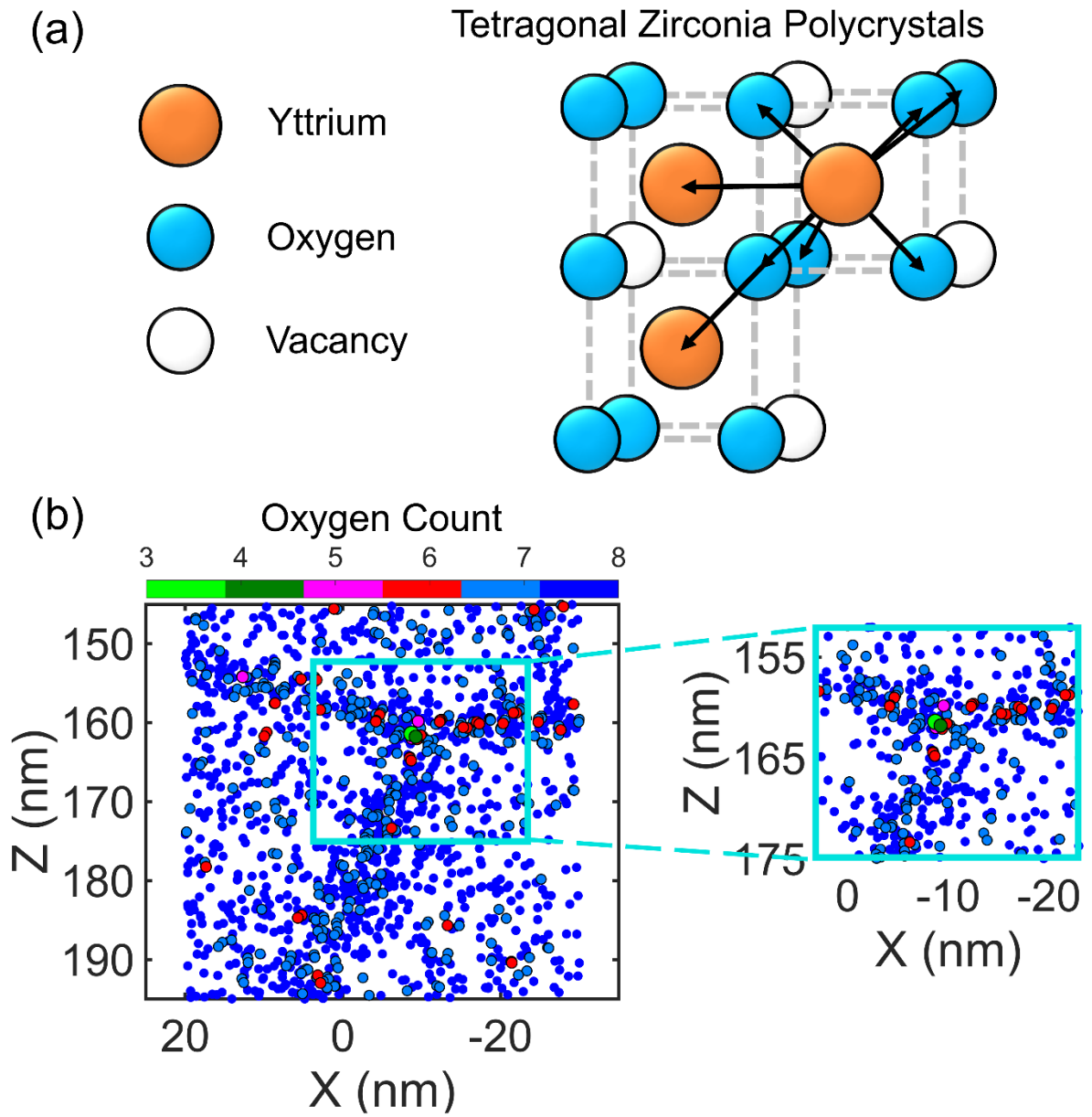
Figure 5: (a) Schematic of the pseudo-coordination number method applied to yttria-stabilized tetragonal zirconia. Arrows indicate the distances from an Y atom to its eight nearest neighbors. (b) Mapping of likely V_Os within the 50 x 50 x 5 nm^3 ROI. Each point is an Y atom. The color of the atom indicates the number of neighboring atoms that contain O. The cropped image (right) provides a close-up of the triple junction contained in the boxed region.

Tables

Table 1. Principal Component (PC) contribution to variability and corresponding feature.

Component	Contribution to variability (%)	Feature	Feature Definition
PC1	63.2	ΔP	Number of pulser firings since the last recorded ion event.
PC2	18.9	Like-NN	Average distance to the first 8 nearest neighbors of the same species.
PC3	13.0	RSS	Root sum squared of the $X_{Detector}$ and $Y_{Detector}$ position.
PC4	5.0	TOF	Time-of-flight
PC5	0.02	V_{DC}	DC voltage

Table 2. Grain Boundary (GB) composition and thickness characterization.

Samples		Sample 1					Sample 2		
Regions		Bulk	GB 1	GB 2	GB 3	GB 4	Bulk	GB 1	GB 2
Composition Light Ions	O at.%	70.8	70.4	70.2	71.7	71.2	70.6	69.7	69.9
	Al at.%	0.05	1.5	0.1	0.0	0.0	0.04	0.1	0.5
	Si at.%	0.02	0.4	0.0	0.0	0.0	0.02	0.0	0.1
Composition Heavy Ions	Zr at.%	27.5	24.1	24.4	23.8	25.4	27.7	25.4	27.3
	Y at.%	1.3	3.3	5.0	4.2	3.1	1.4	4.6	1.9
	Hf at.%	0.3	0.3	0.3	0.3	0.3	0.3	0.2	0.3
Thickness (nm)		-	4.8	9.3	7.0	8.3	-	11.0	7.6

References

[1] F. Zhang, J. Chevalier, C. Olagnon, M. Batuk, J. Hadermann, B. Van Meerbeek, J. Vleugels, J Dent Res 96(7) (2017) 774-779.
[2] I. Denry, J.R. Kelly, Dent Mater 24(3) (2008) 299-307.
[3] C. Piconi, G. Maccauro, Biomaterials 20(1) (1999) 1-25.
[4] H.G. Scott, J Mater Sci 10(9) (1975) 1527-1535.
[5] K. Srivastava, R. Patil, C. Choudhary, K. Gokhale, E. Subba Rao, Trans Brit Ceram Soc 73 (1974) 85-91.
[6] J. Chevalier, L. Gremillard, S. Deville, Annual Review of Materials Research 37 (2007) 1-32.
[7] K. Obal, Z. Pedzich, T. Brylewski, M. Rekas, Int J Electrochem Sc 7(8) (2012) 6831-6845.
[8] R.C. Garvie, R. Hannink, R. Pascoe, Sintering Key Papers, Springer1990, pp. 253-257.
[9] J. Chevalier, A. Liens, H. Reveron, F. Zhang, P. Reynaud, T. Douillard, L. Preiss, V. Sergo, V. Lughi, M. Swain, J Am Ceram Soc 103(3) (2020) 1482-1513.
[10] A. Feder, M. Anglada, J Eur Ceram Soc 25(13) (2005) 3117-3124.
[11] D.L. Porter, A.H. Heuer, J Am Ceram Soc 60(5-6) (1977) 280-281.
[12] P. Pittayachawan, A. McDonald, A. Petrie, J.C. Knowles, Dent Mater 23(8) (2007) 1018-1029.
[13] C. Wei, L. Gremillard, Acta Mater 144 (2018) 245-256.
[14] S. Ramesh, K.Y.S. Lee, C.Y. Tan, Ceram Int 44(17) (2018) 20620-20634.
[15] M.L. Mecartney, M. Ruhle, Acta Metall Mater 37(7) (1989) 1859-1863.
[16] J. Chevalier, Biomaterials 27(4) (2006) 535-543.
[17] V. Lughi, V. Sergo, Dent Mater 26(8) (2010) 807-820.
[18] Q. Jing, J.X. Bao, F. Ruan, X.W. Song, S.L. An, Y.H. Zhang, Z. Tian, H.D. Lv, J.Q. Gao, M. Xie, Ceram Int 45(5) (2019) 6066-6073.
[19] F. Zhang, K. Vanmeensel, M. Inokoshi, M. Batuk, J. Hadermann, B. Van Meerbeek, I. Naert, J. Vleugels, J Eur Ceram Soc 35(2) (2015) 741-750.
[20] K. Matsui, H. Yoshida, Y. Ikuhara, Sci Rep-Uk 4 (2014).
[21] F. Zhang, M. Batuk, J. Hadermann, G. Manfredi, A. Marien, K. Vanmeensel, M. Inokoshi, B. Van Meerbeek, I. Naert, J. Vleugels, Acta Mater 106 (2016) 48-58.
[22] K. Matsui, N. Ohmichi, M. Ohgai, H. Yoshida, Y. Ikuhara, J Mater Res 21(9) (2006) 2278-2289.
[23] J.F. Li, R. Watanabe, J Mater Sci 32(5) (1997) 1149-1153.
[24] A.A. Nogiwa-Valdez, W.M. Rainforth, P. Zeng, I.M. Ross, Acta Biomater 9(4) (2013) 6226-6235.
[25] I.M. Ross, W.M. Rainforth, A.J. Scott, A.P. Brown, R. Brydson, D.W. McComb, J Eur Ceram Soc 24(7) (2004) 2023-2029.
[26] R. Krishnamurthy, Y.G. Yoon, D.J. Srolovitz, R. Car, J Am Ceram Soc 87(10) (2004) 1821-1830.
[27] J. Chevalier, L. Gremillard, A.V. Virkar, D.R. Clarke, J Am Ceram Soc 92(9) (2009) 1901-1920.
[28] J. Chevalier, A. Liens, H. Reveron, F. Zhang, P. Reynaud, T. Douillard, L. Preiss, V. Sergo, V. Lughi, M. Swain, N. Courtois, J Am Ceram Soc 103(3) (2020) 1482-1513.
[29] H. Schubert, F. Frey, J Eur Ceram Soc 25(9) (2005) 1597-1602.
[30] X. Guo, J Mater Sci 36(15) (2001) 3737-3744.
[31] H. Nakajima, T. Mori, Journal of alloys and compounds 408 (2006) 728-731.
[32] X. Guo, R. Waser, Prog Mater Sci 51(2) (2006) 151-210.
[33] X. Guo, Z.L. Zhang, Acta Mater 51(9) (2003) 2539-2547.
[34] B. Feng, N.R. Lugg, A. Kumamoto, Y. Ikuhara, N. Shibata, Acs Nano 11(11) (2017) 11376-11382.
[35] H.B. Lee, F.B. Prinz, W. Cai, Acta Mater 61(10) (2013) 3872-3887.
[36] T. Yokoi, M. Yoshiya, H. Yasuda, Langmuir 30(47) (2014) 14179-14188.
[37] M. Yoshiya, T. Oyama, J Mater Sci 46(12) (2011) 4176-4190.
[38] J.E. Jackson, A user's guide to principal components, John Wiley & Sons2005.

[39] O.G. Licata, S. Broderick, E. Rocco, F. Shahedipour-Sandvik, B. Mazumder, Appl Phys Lett 119(3) (2021).

[40] L. Xu, Y. Xiao, A. van Sandwijk, Q. Xu, Y. Yang, J Nucl Mater 466 (2015) 21-28.

[41] B. Gault, M.P. Moody, J.M. Cairney, S.P. Ringer, Atom probe microscopy, Springer Science & Business Media2012.

[42] N. Kambhatla, T.K. Leen, Neural Comput 9(7) (1997) 1493-1516.

[43] G. Ivosev, L. Burton, R. Bonner, Anal Chem 80(13) (2008) 4933-4944.

[44] W.D. Callister, D.G. Rethwisch, Materials science and engineering: an introduction, 2018.

[45] M. Jimenez-Melendo, A. Dominguez-Rodriguez, Philos Mag A 79(7) (1999) 1591-1608.

[46] M. Jimenez-Melendo, A. Dominguez-Rodriguez, A. Bravo-Leon, J Am Ceram Soc 81(11) (1998) 2761-2776.

[47] K. Kowalski, K. Obal, Z. Pedzich, K. Schneider, M. Rekas, J Am Ceram Soc 97(10) (2014) 3122-3127.

[48] Y.Y. Lei, Y. Ito, N.D. Browning, T.J. Mazanec, J Am Ceram Soc 85(9) (2002) 2359-2363.

[49] K. Suenaga, D. Bouchet, C. Colliex, A. Thorel, D.G. Brandon, J Eur Ceram Soc 18(10) (1998) 1453-1459.

[50] I.M. Ross, W.M. Rainforth, D.W. McComb, A.J. Scott, R. Brydson, Scripta Mater 45(6) (2001) 653-660.